

# Low Noise Signal Processing Technique for Monopulse Pointing of DSN 34-meter Diameter Antennas

MiMi Aung Gudim, Wodek Gawronski  
Jet Propulsion Laboratory  
4800 Oak Grove Dr.  
Pasadena, CA 91109  
(818)354-6987, (818)354-1783

mimi.a.gudim@jpl.nasa.gov, wodek.gawronski@jpl.nasa.gov

**Abstract**— This paper describes a 31.8-32.3 GHz (Ka-band) monopulse antenna pointing system designed to meet a pointing precision requirement of a mean-radial-error (MRE) less than 1.5 milli-degrees for a 34-meter diameter antenna with a 17 milli-degree 3-dB beam-width, under windy conditions up to 15 mph. The high precision is required for the Ka-band radio science experiments requiring high stability in the detected signal power. The physically large system, composed of the antenna, feed, receiving electronics, and the antenna servo controller, is modeled and analyzed as an equivalent phase-locked loop in each axis, azimuth and elevation. The design is also simulated as a two-dimensional system, including the cross-correlation between the two axes. Analysis and simulations agree. From these results, it is summarized that when properly implemented, the technique will meet stated pointing requirement.

## TABLE OF CONTENTS

1. INTRODUCTION
2. KEY DESIGN ISSUES
3. SYSTEM DESIGN
4. SYSTEM ANALYSIS
5. PERFORMANCE ANALYSIS
6. SIMULATION VS. PREDICTED PERFORMANCE
7. CONCLUSION
8. APPENDICES: A, B, C

## 1. INTRODUCTION

In the Deep Space Network (DSN), high precision pointing of very large antennas while receiving very low signal-to-noise ratio (SNR) signals is required to support the Ka-band radio science experiments, for which instability of the detected signal power is required to be less than 0.1 dB due to pointing jitter error. The required pointing precision is a mean-radial-error of less than 1.5 milli-degrees in Ka-band communication, where the 3-dB antenna beam-width is 17 milli-degrees.

Traditionally, the DSN has employed the conical scanning (CONSCAN) algorithm for pointing the antennas at 2.2 to

2.305-GHz (S-band) and 8.2 to 8.6-GHz (X-band). In CONSCAN, the pointing error is estimated by moving the antenna in a circle with respect to the best estimate of the spacecraft location. The received power detected on this circle is used to generate a new best estimate of the spacecraft location. Nominally, the circle chosen is such that the detected power is 0.1 dB less than the peak of the antenna beam. In the beam-waveguide antennas, the 0.1-dB beam widths are 22 mdeg at S-band, 5.9 mdeg at X-Band, and 1.5 mdeg at 31.8 to 32.3-GHz (Ka-band). At S- and X-band frequencies, a typical jitter of 1 mdeg in the antenna pointing (under favorable environmental conditions with no wind) does not result in significant fluctuations in detected power levels. At Ka-band, the same jitter (even without the 15 mph winds) causes significant fluctuations in the detected power levels — not acceptable for radio science application. For this reason, it became necessary to adopt a new technique providing a higher stability.

The selected monopulse pointing method employs a single monopulse feedhorn which is pointed at the best-estimate of the target location. The feedhorn outputs two RF signals: one signal propagates in a  $TE_{11}$  circular-waveguide mode, and the other propagates in a  $TE_{21}$  circular-waveguide mode. These signals are uniquely related in amplitude and phase as a function of the antenna-pointing error. Signal processing electronics are designed to extract the pointing error using the known relationship, and correct the antenna pointing. The single monopulse feed design allows direct pointing at the target at all times, allowing for the spacecraft to be tracked at the peak of the antenna pattern. Use of a single horn makes calibration easier than for the traditional monopulse configuration with three to five feedhorns. An additional advantage is a 0.1-dB gain in signal by not having to point away from the spacecraft as in CONSCAN. This article describes the design and analysis and provides performance predictions for monopulse systems implemented in the DSN 34-meter diameter beam-waveguide (BWG) antennas.

## 2. KEY DESIGN ISSUES

For implementation of a monopulse pointing system in a 34-m-diameter beam-waveguide antennas, challenges lie in the following factors.

*Very low power levels of the received signal:* The received deep-space signals have extremely low power levels due to the small transmission power of a spacecraft and the large distances over which the signal is transmitted.  $P_{c,m}$  can be as low as -160 dBm. To maximize the signal to noise ratio (SNR), ultra-low-noise amplifiers are employed. At Ka-band, these LNAs add 23 degrees Kelvin in the main channel, and 27 degrees Kelvin in the error channel. Because the monopulse pointing-algorithm performance is proportional to the received SNR, the low SNR poses a challenge.

*Large antenna structure:* To receive the very low signal levels, a large antenna aperture, 34 meters in diameter, is required. The large structure is susceptible to vibrations and to deformations due to thermal gradients, azimuth track unevenness, gravity loads, etc. A compensation technique is required to improve the antenna blind pointing. The structure also requires extended pointing performance of the antenna servo system that compensates for the antenna inertia and for flexibility in wind disturbances.

*Distributed downlink system:* The downlink system is distributed in physical distance relative to the frequency of the downlink signal. It introduces relative amplitude and phase distortion in signal routing. The signal-routing distances are up to a few feet at Ka-band frequencies and up to 15~km at the downconverted intermediate frequencies between 100~and 600~MHz.

*High precision pointing-error requirement:* The required amplitude stability of a 0.1-dB gain requires a mean radial error is approximately from 0.7 to 1.5 mdeg due to the narrow width of the Ka-band beam.

Specific perturbation factors that are accounted for in the analysis in this paper are:

- (1) Non-ideal finite null depth in the antenna feed pattern
- (2) Shift in bore sight in the antenna -feed pattern
- (3) Additive (white) noise input
- (4) Wind effect as seen by the encoder
- (5) Encoder error due to discontinuities in the track
- (6) Servo residual error (known)
- (7) Phase-calibration error between the main and error channels

Other sources of noise/perturbation assumed to be negligible in the analysis are:

- (1) Antenna deformation due to lateral and axial displacements due to gravitational force and wind impact on the structure
- (2) Possible asymmetry in the beam-waveguide antenna pattern
- (3) Quantization error
- (4) Doppler dynamics in the target position
- (5) Antenna and feed cross-polarization
- (6) Tracking receiver drift (negligible in a digital receiver)

## 3. SYSTEM DESIGN

The system design is shown in Figure 1. The spacecraft signal at radio frequency (RF) is collected by the 34-m antenna aperture and passed through the single monopulse feed [1]. The outputs of the feed are  $x_m(t)$  and  $x_e(t)$ , the former of which propagates in the  $TE_{11}$  circular-waveguide mode, and the latter propagates in a  $TE_{21}$  circular-waveguide mode respectively. These signals are uniquely related in amplitude and phase as a function of the antenna-pointing error.  $x_m(t)$  and  $x_e(t)$  are independently amplified in two low-noise amplifiers (LNA). The main signal is processed nominally in the receiver algorithms to extract the science data. The error channel is processed, using phase-locked information from the main channel, to estimate the pointing error. The estimated errors are fed to the antenna-pointing servo controller where the detected error is processed, and the antenna position is corrected by the processed amount. This feedback correction closes the monopulse tracking loop.

Figure 1. The monopulse pointing system design

### 3.1 Signal Description

The main and the error signals are  $x_m(t)$  and  $x_e(t)$ :

$$x_m(t) = \sqrt{2P} \cos(\omega_{c,RF} t + \theta_o + \Delta D(t)) + n_m(t) \quad [1]$$

$$x_e(t) = \sqrt{2P} \sqrt{g(\theta_F, \phi_F)} \cos(\omega_{c,RF} t + \theta_c + \Delta D(t) + h(\theta_F, \phi_F)) + n_e(t) \quad [2]$$

where

$P$  = received signal power

$[\omega_{c,RF}, \theta_c]$  = carrier frequency and phase of received signal (at radio frequency)

$\Delta$  = modulation index

$D(t) = d(t) \text{sgn}[\text{Sin}(\omega_{sc} t + \theta_{sc})]$   
= downlink data  $d(t)$  modulated on subcarrier with frequency and phase  $[\omega_{sc}, \theta_{sc}]$

$\theta_F$  = azimuth angle of signal arrival at the feed

$\phi_F$  = elevation angle of signal arrival at the feed

$\sqrt{g(\theta_F, \phi_F)} \cong \gamma \theta_F$   
= ratio of error signal amplitude and main signal amplitude, as a function of  $(\theta_F, \phi_F)$  (see Appendix A)

$\gamma$  = slope of  $\sqrt{g(\theta_F, \phi_F)}$ , sensitivity factor

$h(\theta_F, \phi_F) \cong \phi_F$   
= difference between main and error channel phases, as a function of  $(\theta_F, \phi_F)$  (see Appendix A)

$n_m(t), n_e(t)$  = additive white noise in the main and error channels

After independent amplification and down-conversion to an intermediate frequency (IF) between 100-600 MHz,

$$x_{m,IF}(t) = \sqrt{2P} \cos(\omega_{IF} t + \theta_{IF} + \Delta D(t)) + n_{m,IF}(t) \quad [3]$$

$$\begin{aligned} x_{e,IF}(t) &= \sqrt{2P} A \sqrt{g(\theta_F, \phi_F)} \cos(\omega_{IF} t + \theta_{IF} + \Delta D(t) \\ &\quad + h(\theta_F, \phi_F) + \Delta\phi) + n_{e,IF}(t) \\ &\cong \sqrt{2P} A \gamma \theta_F \cos(\omega_{IF} t + \theta_{IF} + \Delta D(t) + \phi_F + \Delta\phi) + n_{e,IF}(t) \end{aligned} \quad [4]$$

where

$(\omega_{IF}, \theta_{IF})$  = carrier intermediate frequency and phase

$n_{m,IF}(\cdot), n_{e,IF}(\cdot)$  = received additive noise at the IF

$\Delta\phi$  = relative phase distortion introduced by independent amplification, downconversion and signal routing

$A$  = Relative amplitude distortion between main and error channels introduced by independent amplification, downconversion and signal routing of  $x_m(t), x_e(t)$  respectively.

The ultra-low-noise amplifiers in the system minimize  $n_{m,IF}(\cdot), n_{e,IF}(\cdot)$  to maximize the SNR of the IF signals  $x_{m,IF}(t)$  and  $x_{e,IF}(t)$  which are processed in the receiver as shown in Figure 2 and described in Appendix B. The main channel processes the signal for the spacecraft data, and aids the error channel to estimate the pointing error. The

outputs from the error channel after normalization and de-rotation to match the coordinates for the servo controller, are the estimates of the pointing error in azimuth and elevation, which can be expressed as:

$$\begin{bmatrix} \hat{az\_err}(t) \\ \hat{el\_err}(t) \end{bmatrix} = A_\Lambda \begin{bmatrix} \cos(\phi_\Delta) & -\sin(\phi_\Delta) \\ \sin(\phi_\Delta) & \cos(\phi_\Delta) \end{bmatrix} \begin{bmatrix} az\_err(t) \\ el\_err(t) \end{bmatrix} + \begin{bmatrix} n_{az}(t) \\ n_{el}(t) \end{bmatrix} \quad [5]$$

where

$A_\Lambda$  = total amplitude normalization error

$\phi_\Delta$  = total phase calibration error

Figure 2. Block diagram of receiver signal processing

The estimated vector  $\hat{\bar{z}} = \begin{bmatrix} \hat{az\_err}(t) \\ \hat{el\_err}(t) \end{bmatrix}$  is equal to the true vector  $\bar{z} = \begin{bmatrix} az\_err(t) \\ el\_err(t) \end{bmatrix}$  scaled by  $A_\Lambda$  and rotated in 2-dimensional space by angle  $\phi_\Delta$ , with an added noise vector  $\begin{bmatrix} n_{az}(t) \\ n_{el}(t) \end{bmatrix}$  as illustrated in Figure 3.

Figure 3. The estimated versus true pointing error vectors.

The estimated pointing error values  $\begin{bmatrix} \hat{a}z\_err(t) \\ \hat{e}l\_err(t) \end{bmatrix}$  are fed into the servo controller where they are processed. To combat the effects of wind, an aggressive controller design, the Linear-Quadratic-Gaussian (LQG) controller, is adopted [2][3]. The processed values are used to correct the position of the antenna, thus closing the monopulse loop.

### 3.2 Behavioral Description of the Two-Dimensional Monopulse Loop

The Monopulse system can be modeled as a two-dimensional feed-back system in azimuth and elevation. Given the pointing error vector  $\vec{Z}$ , applying an ideal correction vector  $\vec{C} \equiv -\vec{Z}$  will reduce the error to zero (Figure 4(a)). For this case, the two-dimensional acquisition process is shown in Figure 4(b) where "X" marks the target, and the origin represents the initial antenna point. The dashed line shows the instantaneous position of antenna pointing en route to the target. The dashed line in this case follows a direct path to acquiring lock onto the target.

Figure 4. The ideal case for pointing correction: (a) perfect pointing correction in two-dimensional space and (b) ideal transient response in target acquisition.

However, with the estimated pointing error shown in described Equation [5],  $\vec{C} = \vec{Z}$  reduces but not perfectly compensate for  $\vec{Z}$ , as illustrated in Figure 5(a). With each feedback indexed "i", the 2-D pointing error will decrease in magnitude as long as the following holds:

$$|\vec{Z}_{i+1}| = |-\mathbf{A}_\Lambda \vec{Z}_i + \vec{n}_i - \vec{Z}_i| < |\vec{Z}_i| \quad [6]$$

i.e. if the following holds:

$$|\vec{n}_i - (\mathbf{A}_\Lambda - \mathbf{I}) \vec{Z}_i| < |\vec{Z}_i|$$

For this case, the pointing error is corrected in a meandering pattern that converges near the target as shown in Figure 5(b). At some point along the decreasing  $|\vec{Z}_i|$  process, the noise amplitude exceeds the needed correction and above condition is no longer valid. At this point, the error  $\vec{Z}$  will wander within a circle of radius  $\theta_{o,max}$  which is a function of the noise characteristics,  $\vec{n}_i$ .

Figure 5. The non-ideal case for pointing correction: (a) imperfect pointing correction in two-dimensional space and (b) non-ideal transient response in target acquisition.

In summary, given an initial pointing error  $\vec{Z}_0$ , the monopulse loop recursively reduces the error through feedback until the noise limit is reached. At that point, the pointing error wanders within the noise limit radius  $\theta_{o,max}$  which represents the performance limit of the loop.

## 4. SYSTEM ANALYSIS

A block diagram of the monopulse system signal processing design is shown in Figure 6.

Figure 6. The monopulse signal processing design.

#### 4.1 Equivalent Analytical Model

Assuming independence between the azimuth and elevation axes of the antenna and feed, the system can be analyzed as being composed of two equivalent phase-locked loops (PLL) [4] shown in Figure 7.

$$H_m[s] \equiv \frac{\Theta_{out}[s]}{\Theta_{in}[s]} \quad [7]$$

with noise equivalent bandwidth  $B_{L,m}$ .

(2) Disturbance transfer function, between the servo noise location and the output is defined as:

$$H_r[s] \equiv \frac{\Theta_{out}[s]}{\Theta_{in, servo}[s]} \quad [8]$$

with noise equivalent bandwidth  $B_{L,r}$ .

For the DSN BWG antennas,

$$H_m[s] = \text{ADD ACTUAL 15-PARAMS} \quad [9]$$

$$\equiv \frac{\omega_o^2}{s^2 + 2\xi\omega_o s + \omega_o^2}$$

$$H_r[s] = \text{ADD ACTUAL 15-PARAMS}$$

$$\equiv \frac{2\xi\omega_o s}{s^2 + 2\xi\omega_o s + \omega_o^2} \quad [10]$$

where

$$\omega_o = \sqrt{\frac{k}{T}}$$

$$\xi = \frac{1}{2\sqrt{kT}}$$

where  $k$  and  $T$  are second order loop parameters. The parameters are as shown in Table 1. For the very large antenna system, this system employs an aggressive servo controller to achieve a relatively large bandwidth (0.4 Hz) to combat wind perturbations.

Table 1. LQG controller parameters for DSN BWG antennas

$T$ (sec)	$k$ (sec <sup>-1</sup> )	$\omega_o$ (rad)	$f_o$ (Hz)	$\xi$	$B_{L,m}$ (Hz)	$B_{L,r}$ (Hz)
0.159	1	2.51	0.4	1.25	0.4	0.4

#### 5. PERFORMANCE ANALYSIS

In the following two subsections, performance of the monopulse loop is assessed in terms of (1) transient response in acquiring the target, and (2) statistical expectation of error jitter in estimates of the cross-elevation and elevation pointing after target acquisition.

Figure 7. Analytical model of the monopulse loop: (a) elevation tracking loop and (b) azimuth tracking loop.

The dashed circles show the system perturbations and their injection points into the system. Each loop is analogous to a PLL in the following sense:

- (1) The combination of the antenna, the feed, and the receiver signal processing chain is analogous to the combination of the phase-error detector and the follow-on integrator for improved SNR in a PLL.
- (2) The servo controller in the APC is analogous to the PLL loop-filter.
- (3) The combination of the servo controller and antenna correction is analogous to the numerically controlled oscillator (NCO) and feedback in a PLL.

As such, the loop jitter on the estimated pointing error is the sum of individual contribution from each of the noise components injected into the loop. The individual contribution of each perturbation is filtered through the transfer function between the point of injection and the output of the loop. For evaluation of each component, the following transfer functions and bandwidths are defined:

- (1) Transfer function between the input and the output:

### 5.1 Non-ideal Transient Response

Non-ideal transient response in acquiring the target pointing described in Section 3.2 can be caused by the following factors in the system.

**5.1.1 Bore-sight shift in antenna/feed pattern** — The bore-sight shift, described in Appendix A, will result in the system acquiring the target with a constant error offset.

**5.1.2 Calibration between  $x_m(\cdot)$  and  $x_e(\cdot)$**  — Independent low-noise amplification, RF-to-IF downconversion, and signal routing also contributes to the amplitude and phase imbalance ( $A$ ,  $\Delta\phi$ ) between the main and the error channels. These components are to be calibrated as closely as possible in the implementation. Residual phase imbalance leads to a longer acquisition time as the loop tracks through an indirect route to the lock point, as described in Section 3.2 [see Fig.~5(b)].

### 5.2 Pointing-Error Jitter after Target Acquisition

After target acquisition, the system will be locked onto the target with a jitter due to the noise components in the system. The system design goal is to minimize the jitter. The jitter will be assessed in terms of the mean-radial-error (MRE) defined as:

$$\text{MRE} \equiv E[\sqrt{(\text{xeloff} - \hat{\text{xeloff}})^2 + (\text{eloff} - \hat{\text{eloff}})^2}] \quad [11]$$

where  $E[\cdot]$  denotes statistical expectation.

For DSN BWG antennae, the MRE is coarsely approximated as<sup>1</sup>:

$$\text{MRE} \approx \sqrt{\frac{\pi}{2}} \sqrt{\frac{1}{2}(\sigma_{\text{xel}}^2 + \sigma_{\text{el}}^2)}, \quad [12]$$

The standard deviations of errors,  $\sigma_{\text{xel}}$  and  $\sigma_{\text{el}}$ , in the  $\text{xel}_{\text{off}}$  and  $\text{el}_{\text{off}}$  estimates, respectively, are approximated by the root of the sum of the squares (RSS) of the independent perturbations in the equivalent loop shown in Figure 9, i.e.,

<sup>1</sup> In the coarse approximation, it is assumed that  $(\text{xel}_{\text{off}} - \hat{\text{xel}}_{\text{off}})$  and  $(\text{el}_{\text{off}} - \hat{\text{el}}_{\text{off}})$  are Gaussian-distributed random variables, and the approximation is an extrapolation from the case when variables  $X$  and  $Y$  are equally distributed and Gaussian, i.e.,  $\sigma_{\text{single axis}}^2 \equiv \text{Var}[X] = \text{Var}[Y]$ , where the term  $\sqrt{X^2 + Y^2}$  can be approximated as a Raleigh distribution sample with a mean of  $\sqrt{\frac{\pi}{2}}\sigma_{\text{single axis}}$  and a variance of  $(2 - \frac{\pi}{2})\sigma_{\text{single axis}}^2$

$$\sigma_{\text{xel}} = \sqrt{\frac{\sigma_{\text{limit-cyc}}^2}{2} + \sigma_{\text{sys noise}}^2 + \sigma_{\text{servo}}^2 + \sigma_{\text{enc}}^2 + \sigma_{\text{wind,AZ}}^2} \quad [13]$$

$$\sigma_{\text{el}} = \sqrt{\frac{\sigma_{\text{limit-cyc}}^2}{2} + \sigma_{\text{sys noise}}^2 + \sigma_{\text{servo}}^2 + \sigma_{\text{wind,EL}}^2} \quad [14]$$

where

$\sigma_{\text{limit-cyc}}^2$  = pointing error due to limit-cycling caused by finite null-depth in antenna /feed pattern

$\sigma_{\text{sys noise}}^2$  = pointing error due to the additive white noise at the input of the monopulse system

$\sigma_{\text{servo}}^2$  = pointing error due to servo noise

$\sigma_{\text{enc}}^2$  = pointing error due to encoder imperfections

$\sigma_{\text{wind,AZ}}^2$  = pointing error in Azimuth axis due to wind disturbances

$\sigma_{\text{wind,EL}}^2$  = pointing error in Elevation axis due to wind disturbances

Each component in Equations [13] and [14] is analyzed individually in the following subsections

**5.2.1 Limit-cycling ( $\sigma_{\text{limit}}^2$ )** — Limit-cycling results from a non-ideal null-depth which is due to: (1) decrease in slope near  $\theta = 0$  and (2) non-negligible feedback value near  $\theta = 0$ . See Appendix A for the full derivation. Jitter on the monopulse loop due to this non-zero value is:

$$\sigma_{\text{limit}}^2 \cong \frac{\theta_{\text{limit}}^2}{2} \quad [15]$$

For DSN BWG antennas,

$$\theta_{\text{limit}}(N') = 0.0014 \times 10^{-\frac{N'(dB)}{20}} \quad [16]$$

**5.2.2 System Noise ( $\sigma_{\text{sys noise}}^2$ )** — Phase jitter due to additive noise at the input of the system, analyzed in Appendix C, is

$$\sigma_{\text{sys noise}}^2 = \frac{1}{\hat{\gamma}^2} R_{\text{BVR}} \left( \frac{A}{\hat{A}} \right)^2 \times \frac{N_{o,s} B_{L,m}}{P_{c,m}} \quad [17]$$

This component is the largest contributor to the total loop performance. It is inversely proportional to the ratio of the signal in the main channel to the noise in the error channel.

5.2.3 *Servo Jitter* ( $\sigma_{servo}^2$ ) — Servo jitter is a noise in the servo loop, observed even if no apparent disturbances, such as wind gusts, are detected. Its contribution to the monopulse pointing jitter is given as:

$$\sigma_{servo}^2 \cong N_{o,servo} B_{L,r} \quad [18]$$

where

$N_{o,servo}$  = the spectral density of the servo noise

5.2.4 *Wind Disturbances* ( $\sigma_{wind}^2$ ) — The wind disturbance model is taken from the field measured data [5] and  $\sigma_{wind,AZ}^2$  and  $\sigma_{wind,EL}^2$  are derived from running the wind model through the monopulse loop model.

5.2.5 *Encoder Imperfections* ( $\sigma_{enc}^2$ ) —  $\sigma_{enc}^2$  in Equation [13] is jitter contribution due to azimuth encoder imperfection. Originally, components of non-linearity consisted of the radial run-out error, manufacturing tolerances, and rapid changes due to the gaps between the encoder rack segments. Recently, the gaps were eliminated by installing a solid one piece encoder rack, consequently reducing  $\sigma_{enc}^2$  significantly.

## 6. PREDICTED AND SIMULATED PERFORMANCE DATA

In this section, the predicted and simulated performances for the 34-m BWG antennas are compared. The predicted values are evaluated from Equations (12), (13), and (14). The simulation results presented are obtained from the two-dimension simulations made using the equivalent model shown in Figure 8.

Figure 8. Block diagrams of (a) the nonlinear monopulse control model and (b) the monopulse pointing error detector

The azimuth and elevation axes were simulated jointly, portraying the weak correlation that exists due to the feed patterns being functions of both axes. Other physical and/or structural correlations that may exist were not included. The simulation included predicted antenna patterns, the signal-processing equations, and the actual servo filter parameters. Measured values of wind and servo jitter were injected into the simulation. For the encoder non-linearity,  $\sigma_{enc}^2$  in Equation (13) was derived from measured values of the segmented encoder gear rack run through a model of the monopulse loop. Since the segmented problem has been reduced significantly (see Section 5.1.5), the predicted and simulated results in this article are pessimistic.

In the following subsections, the predicted and simulated mean radial errors are shown for

null depth = 35 dB and 15 dB

$B_{L,m} = B_{L,r} = 0.4$  Hz

phase calibration

error in entire loop = 25 deg

bore-sight shift = 0.5 mdeg

$\sigma_{enc} = 0.1$  mdeg (highly pessimistic based upon the new segmented encoder design)

$\sigma_{servo} = 0.1$  mdeg (based upon measured statistics)

wind input = injected field-measured (24 km/h) wind model into the simulation

$$\frac{P_{c,m}}{N_{o,e}} \text{ (dB-Hz)} = \text{variable}$$

### 6.1 Predicted versus Simulated Plots of Monopulse Loop Behavior

In Figure 9, simulation results confirming the loop behavior discussed in Section 3.2 (Figure 5(b)) are shown for various SNRs. In the simulation, the antenna acquires the target at  $az = 5$  mdeg,  $el = 5$  mdeg, starting from the origin in the ( $az, el$ ) plane. Figures 11(a) through (d) show the transient acquisition response path and lock points of

the system for a decreasing value of SNR,  $\frac{P_{c,m}}{N_{o,e}} = \{40, 27,$

$23, 17\}$  dB-Hz. As expected, the radius of the noise limit increases with a decrease in SNR. The acquisition path does not follow a straight line to the target due to the 25-deg phase-calibration error. After acquisition, pointing error wanders randomly within a circle about the target. The size of this circle indicates the extent of the mean radial error, which clearly increases with decrease in the SNR.

null depth of 35 dB and 15 dB, respectively. The predicted and simulated MRE errors agreed well for a null depth of 35 dB. For 15 dB, the prediction was slightly pessimistic as compared with the simulated output.

Figure 9. Pointing error transient response during acquisition and after lock for a  $\frac{P_{c,m}}{N_{o,e}}$  of (a) 40 dB-Hz, (b) 27 dB-Hz, (c) 23 dB-Hz, and (d) 17 dB-Hz.

In Figure 10(a) through (d), simulated measures of radial error as a function of time are shown  $\frac{P_{c,m}}{N_{o,e}} = \{40, 27, 23, 17\}$  dB-Hz. As expected, the mean of the radial error increased with decrease in the SNR.

Figure 10. Pointing radial error as a function of time for a  $\frac{P_{c,m}}{N_{o,e}}$  of (a) 40 dB-Hz, (b) 27 dB-Hz, (c) 23 dB-Hz, and (d) 17 dB-Hz.

## 6.2 Predicted versus Simulated Mean Radial Error

Predicted versus simulated mean radial errors are summarized in Figures 11 and 12 as a function of SNR for a

Figure 11. The predicted compared to the simulated mean radial error for a 35-dB null depth as a function of SNR =  $\frac{P_{c,m}}{N_{o,e}}$

Figure 12. The predicted compared to the simulated mean radial error for a 15-dB null depth as a function of SNR =  $\frac{P_{c,m}}{N_{o,e}}$

## 6.3 Summary of Performance Results

The results given in this section confirm the analytically described loop behavior discussed in Section 3.2. These results also show that the prediction model is reasonable, and they confirm that the Cassini radio science requirement of an MRE less than or equal to 1.5 mdeg can be met down to approximately 17 dB-Hz in  $\frac{P_{c,m}}{N_{o,e}}$ . The simulation model also is useful for testing sensitivity of the loop to various imperfections and perturbations that are encountered during implementation.



## 7.0 CONCLUSION

In this article, a monopulse pointing technique employed for pointing a 34-meter diameter antenna is modeled and analyzed. Acquisition and tracking behavior of the system are described. Pointing performance is characterized in terms of the variance of the mean radial pointing error after target acquisition. Simulation results obtained from two-axes simulation in azimuth and elevation showed agreement with the predicted results. The analysis, simulation, and design presented in this article serve as a good performance prediction as well as a useful aid to identifying implementation errors that can contribute to degradation of the performance. The simulation model can be further utilized to test for sensitivity of the loop to any obvious imperfections encountered in implementation. Results show that, when properly implemented, this technique will meet the Cassini radio science requirement of an MRE less than or equal to 1.5 mdeg down to reasonable SNRs.

Further work to more closely characterize the imperfections in the single-feed monopulse feed-horn pattern will be useful. These patterns can be incorporated in to the simulation models developed for this work. Another area of further work is in designing more aggressive servo filters that can increase the bandwidth of the monopulse loop, which will allow the system to combat even stronger wind perturbations.

## REFERENCES

- [1] Y. H. Choung, K. R. Goudey, and L. G. Bryans, "Theory and Design of a Ku-Band TE<sub>21</sub>-Mode Coupler," *IEEE Transactions on Microwave Theory and Techniques*, vol. 30, No. 11, November 1982.
- [2] W. Gawronski, C. Racho, J. Mellstrom, "Application of the LQG and Feedforward Controllers for the DSN Antennas," *IEEE Trans. on Control Systems Technology*, vol. 3, 1995.
- [3] Gawronski, W. and M. A. Gudim, "Design and Performance of the Monopulse Control System," *Telecommunications and Mission Operations Progress Report 42-137, January-March 1999*, Jet Propulsion Laboratory, Pasadena, California, pp. 1-15, May 15, 1999.
- [4] F. M. Gardner, "Phaselock Techniques," *John Wiley & Sons, Inc.*, 1979.
- [5] Gawronski, W., "Wind Gust Models Derived From Field Data," *Telecommunications and Data Acquisition Progress Report 42-123, July-September 1995*, Jet Propulsion Laboratory, Pasadena, California, pp. 30-36, November 15, 1995.

## APPENDIX A

### ANTENNA-FEED PATTERNS

The antenna and feed combined (antenna/feed) dictate the amplitude and phase relationship between the received  $x_m(t)$  and  $x_e(t)$  through  $\sqrt{g(\theta_F, \phi_F)}$  and  $h(\theta_F, \phi_F)$  in Equations [1] and [2] of the main text.  $h(\theta_F, \phi_F)$  is the phase response in the signal component of the received signal, and  $\sqrt{g(\theta_F, \phi_F)}$  is the amplitude response in the signal component of the received  $x_e(t)$ .

Plots of  $\sqrt{g(\theta_F, \phi_F)}$  and  $h(\theta_F, \phi_F)$  predicted for the DSN beam-waveguide (BWG) antennae are shown in Figure A-1 for the ideal case where

$$(i) \quad h(\theta_F, \phi_F) \cong \phi_F \quad (\text{Figure A-1(e)}) \quad [A-1]$$

$$(ii) \quad \sqrt{g(\theta_F, \phi_F)} \cong \gamma \theta_F \quad (\text{Figure A-1(f)}) \quad [A-2]$$

In the ideal case, the slope of  $\sqrt{g(\theta_F, \phi_F)}$ ,  $\gamma(\theta, \phi)$ , is a constant:

$$\gamma(\theta, \phi) \equiv \frac{d}{d\theta} = \gamma \quad [A-3]$$

$x_e(t)$  is composed of the signal component proportional to  $\theta_F$  by the proportionality factor  $\gamma$ , and a noise component that is independent of  $\gamma$ . Therefore, the larger the value of  $\gamma$ , the larger the signal-to-noise ratio of the received signal.  $\gamma$  is an intrinsic parameter depending on implementation of the antenna and feed. The implementation goal is achieve as large a value of  $\gamma$  as possible. For the DSN BWG antennae,  $\gamma \cong 70 \text{ V/V/deg}$  (Volt per Volt per degree).

#### A.1 Null-depth of the antenna/feed pattern

Null-depth of the antenna/feed pattern is defined as the ratio of the peak to valley of  $g(\theta_F, \phi_F)$ :

$$N[\text{dB}] \equiv 10 \text{ Log}_{10} \left[ \frac{g(\theta_{F, \max}, \phi_F)}{g(\theta_{F, \min}, \phi_F)} \right] \quad [A-4]$$

**Ideal null-depth** — In the ideal case, null-depth is infinite.

**Non-ideal null-depth** — In the non-ideal case, the null-depth is finite and  $\sqrt{g'(\theta_F, \phi_F)}$  is non-linear near  $\theta_F \cong 0$ .

In our analysis, the non-ideal null-depth was modeled as the ideal null-depth degraded by addition of a constant, representing a constant offset in DC.

$$g'(\theta_F, \phi_F) = \gamma^2 \theta_F^2 + g_{off}(N') \quad [A-5]$$

where

$g_{off}(N')$  = a constant as a function of  $N'$ . A plot of  $\sqrt{g'(\theta_F, \phi_F)}$  for null-depth of 15 dB is shown in Figure A-2. In this case, the slope of  $\sqrt{g'(\theta_F, \phi_F)}$  is a function of  $(\theta_F, \phi_F)$ , rather than a constant:

$$\gamma(\theta_F, \phi_F, N') = \frac{d}{d\theta} \sqrt{g'(\theta_F, \phi_F)} = \frac{a^2 \theta_F}{\sqrt{a^2 \theta_F^2 + g_{off}(N')}} \quad [A-6]$$

Aside:

For simulation purposes, the model used was:

$$g_{off}(N'(dB)) = 10^{-\left[0.5 + \frac{N'(dB)}{10}\right]} - g(\theta_{min}, \phi) \quad [A-7]$$

$$\cong 10^{-\left[0.5 + \frac{N'(dB)}{10}\right]}$$

A reasonable assumption made in the above derivation is:

$$g_{off} \ll g(\theta_{max}, \phi) \times 10^{-5} \quad [A-8]$$

#### *Degradation to the Monopulse Loop Performance due to Non-ideal Antenna/Feed Patterns*

Two types of degradation to the Monopulse loop occur due to non-ideal antenna/feed patterns. They are: limit-cycling and boresight shift.

##### *A.2 Limit-Cycling*

Limit-cycling is a degradation in the Monopulse loop due to a non-ideal null-depth causing:

- decrease in slope near  $\theta = 0$
- non-negligible feedback value near  $\theta = 0$

To demonstrate this, for  $a = 70.6$  V/V/deg (which is the case for DSS 25),  $\sqrt{g'(\theta_F, \phi_F)}$  is plotted for  $N' = 15, 20, 25, 30, 35$  dB in Figure A-3. From the figure, it is seen that there exists  $\gamma_{limit}$  such that for each  $N'$ , there is a corresponding  $\theta_{limit}$ , below which the loop cannot drive error smaller because of insufficient gain and non-zero

feedback value about  $\theta=0$ . Jitter on the Monopulse loop due to this inability to reach zero is:

$$\sigma_{limit}^2 \cong \frac{\theta_{limit}^2}{2} \quad [A-9]$$

For DSS 25,

$$\theta_{limit}(N') \cong 0.0014 \times 10^{-\frac{N'(dB)}{20}} \quad [A-10]$$

##### *A.3 Boresight shift*

Boresight shift may be caused by misalignment between the antenna and the feed in implementation, where the RF peak and the null of the antenna pattern are offset by  $\theta_{b.s.}$  as shown in Figure A-4. Such an error is expected to be negligible for the 34-m beam-waveguide antenna implementation, but is discussed here for completeness. This boresight shift will move the lock point of the monopulse loop to  $\theta_{b.s.}$  away from the RF peak. No significant contribution to the pointing jitter is expected at the lock point.

## APPENDIX B

### RECEIVER SIGNAL PROCESSING

In this Appendix, the IF receiver signal processing, shown in Figure 2, is described. The signals after low-noise amplification are:

$$x_{m,LNA}(t) = \sqrt{2P} \cos(\omega_{c,RF} t + \theta_c + \Delta D(t)) + n_{m,LNA}(t) \quad [B-1]$$

$$x_{e,LNA}(t) = \sqrt{2P} A_1 \sqrt{g(\theta_F, \phi_F)} \cos(\omega_{c,RF} t + \theta_c + \Delta D(t) + \Delta\phi' + h(\theta_F, \phi_F)) + A_1 n_{e,LNA}(t) \quad [B-2]$$

where

$A_1$  = relative amplitude distortion between main and error channels introduced by independent amplification

$\Delta\phi'$  = relative phase distortion between main and error channels introduced by independent amplification

$n_{m,LNA}(t), n_{e,LNA}(t)$  = additive white noise at output of LNAs, with noise spectral density of  $N_{o,m}$  and  $N_{o,e}$  respectively.

These signals are individually downconverted to intermediate frequency (IF):

$$x_{m,IF}(t) = \sqrt{2P} \cos(\omega_{IF} t + \theta_{IF} + \Delta D(t)) + n_{m,BVR}(t) \quad [B-3]$$

$$x_{e,IF}(t) = A \sqrt{2P} \sqrt{g(\theta_F, \phi_F)} \cos(\omega_{IF} t + \theta_{IF} + \Delta D(t) + h(\theta_F, \phi_F) + \Delta\phi) +$$

$$A n_{e,BVR}(t) \quad [B-4]$$

where

$(\omega_{IF}, \theta_{IF})$  = carrier intermediate frequency and phase

$n_{m,IF}(\cdot)$ ,  $n_{e,IF}(\cdot)$  = received additive noise after the ultra-low-noise amplification

$\Delta\phi$  = relative phase distortion between main and error channels introduced by independent amplification, downconversion and signal routing of  $x_{m,IF}(t)$ ,  $x_{e,IF}(t)$  respectively

$A$  = relative amplitude distortion between main and error channels introduced by independent amplification, downconversion and signal routing of  $x_{m,IF}(t)$ ,  $x_{e,IF}(t)$  respectively

At the IF, the signal is digitized and the main signal,  $x_{m,BVR}(t)$ , is tracked by the standard phase-locked loop. The error signal,  $x_{e,BVR}(t)$ , is demodulated in-phase and in-quadrature at the frequency and phase estimated in the main loop. The demodulation signals are:

$$\begin{aligned} x_{\text{demod,cos}}(t) &= \cos(\hat{\omega}_{IF} t + \hat{\theta}_{IF} + n_{\phi_e}(t) + \Delta\hat{\phi}) \\ &\cong \cos(\hat{\omega}_{IF} t + \hat{\theta}_{IF} + \Delta\hat{\phi}) \end{aligned} \quad [B-5]$$

$$\begin{aligned} x_{\text{demod,sin}}(t) &= \sin(\hat{\omega}_{IF} t + \hat{\theta}_{IF} + n_{\phi_e}(t) + \Delta\hat{\phi}) \\ &\cong \sin(\hat{\omega}_{IF} t + \hat{\theta}_{IF} + \Delta\hat{\phi}) \end{aligned} \quad [B-6]$$

where  $n_{\phi_e}(t)$  is the noise in main loop carrier tracking, with standard PLL phase jitter [4]:

$$\text{Var}[n_{\phi_e}(t)] = \frac{1}{\text{SNR}_{L,\text{main}}} = \frac{N_{o,m} B_{L,m}}{P_{c,m}} \quad [B-7]$$

$P_{c,m}$  = carrier power at the input of the main carrier tracking loop

$B_{L,m}$  = bandwidth of the main loop

The demodulated signals prior to normalization are:

$$\begin{aligned} \hat{f}'_{\text{eloff}}(t) &= [x_{e,IF}(t) x_{\text{demod,Sin}}(t)]_{\text{LPF}} \\ &\cong -\frac{1}{2} A \sqrt{2P} \gamma \theta_F \sin(\phi_F + \Delta\phi_{\text{calib}}) + [n_{e,IF}(t) x_{\text{demod,Cos}}(t)]_{\text{LPF}} \end{aligned} \quad [B-8]$$

where

$$n'_{fel}(t) = [n_{e,BVR}(t) x_{d,Cos}(t)]_{\text{LPF}}$$

$\Delta\phi_{\text{calib}}$  = uncalibrated phase error between main and error channels  
 $= \Delta\phi' - \Delta\hat{\phi}$

$$\begin{aligned} \hat{f}'_{\text{eloff}}(t) &= [x_{e,IF}(t) x_{\text{demod,Cos}}(t)]_{\text{LPF}} \\ &\cong \frac{1}{2} A \sqrt{2P} \gamma \theta_F \cos(\phi_F + \Delta\phi_{\text{calib}}) + [n_{e,IF}(t) x_{\text{demod,Sin}}(t)]_{\text{LPF}} \end{aligned} \quad [B-9]$$

where

$$n'_{fel}(t) = [n_{e,IF}(t) x_{\text{demod,Cos}}(t)]_{\text{LPF}}$$

The signals are normalized by:

$$\hat{K} = \frac{1}{2} \hat{A} \sqrt{2\hat{P}} \hat{\gamma}$$

where

$\hat{A}$  = estimated amplitude calibration

$\sqrt{2\hat{P}}$  = estimated signal amplitude from the main signal loop, assuming that

$$\sqrt{2\hat{P}} + n_{PLL}(t) \cong \sqrt{2\hat{P}} \text{ in the main PLL}$$

$\hat{\gamma}$  = estimated slope of S-curve

Normalized estimates of elevation and cross-elevation errors are:

$$\hat{f}'_{\text{xeloff}}(t) = -R_{BVR} \theta_F \sin(\phi_F + \Delta\phi_{\text{calib}}) + n_{fxel}(t) \quad [B-10]$$

$$\hat{f}'_{\text{eloff}}(t) = R_{BVR} \theta_F \cos(\phi_F + \Delta\phi_{\text{calib}}) + n_{fel}(t) \quad [B-11]$$

where

$$\begin{aligned} R_{BVR} &= \frac{A \gamma \sqrt{P}}{\hat{A} \hat{\gamma} \sqrt{\hat{P}}} \\ n_{fxel}(t) &= \frac{n'_{fxel}(t)}{\hat{K}} \\ n_{fel}(t) &= \frac{n'_{fel}(t)}{\hat{K}} \end{aligned}$$

After appropriate normalization to map to the antenna servo coordinates, the output of the IF processing in matrix format is:

$$\begin{bmatrix} \hat{az\_err}(t) \\ \hat{el\_err}(t) \end{bmatrix} = A_{\Lambda} \begin{bmatrix} \cos(\phi_{\Delta}) & -\sin(\phi_{\Delta}) \\ \sin(\phi_{\Delta}) & \cos(\phi_{\Delta}) \end{bmatrix} \begin{bmatrix} az\_err(t) \\ el\_err(t) \end{bmatrix} + \begin{bmatrix} n_{az}(t) \\ n_{el}(t) \end{bmatrix} \quad [B-12]$$

## APPENDIX C

### SYSTEM NOISE ANALYSIS [C-8]

Pointing error jitter contribution due to the additive white noise at the input of the monopulse system is evaluated in

the section as  $\sigma_{sys-noise}^2$  .  $\sigma_{sys-noise}^2$  is the same in cross-elevation and elevation axes because the their equivalent models are the same. The system noise jitter contribution is

$$\begin{aligned}\sigma_{sys-noise}^2 &= N_{0,BVR-out} B'_{L,m} \\ &= \frac{1}{\gamma^2} R_{BVR} \left( \frac{A}{\hat{A}} \right)^2 \times \frac{N_{0,e} B_{L,m}}{P_{c,m}}\end{aligned}\quad [C-1]$$

where

$B'_{L,m}$  = equivalent bandwidth of the monopulse

loop

$$= B_{L,m} \times R_{BVR}$$

$N_{0,BVR-out}$  = spectral density of additive noise after BVR processing

$$= 2T_{upd} \times \text{Var}[n_{f,el}(\cdot)] = 2T_{upd} \times \text{Var}[n_{f,xel}(\cdot)]$$

$$\text{Var}[n_{fel}(t)] = \text{Var}[n_{fxel}(t)]$$

$$= \frac{1}{2} \left( \frac{A}{\hat{K}} \right)^2 \text{Var}[n_{e,LNA}(\cdot)] \quad [C-2]$$

$$= \frac{1}{2} A^2 \frac{N_{0,e}}{2T_s} \left( \frac{1}{\frac{1}{2} \hat{A} \sqrt{2\hat{P}} \hat{\gamma}} \right)^2 \frac{f_{upd}}{f_s}$$

$$\text{Var}[n_{e,LNA}(\cdot)] \equiv \frac{N_{0,e}}{2T_s}$$

$f_s = 1/T_s$  = the sampling rate of the receiver

$f_{upd} = 1/T_{upd}$  = the sampling rate of the monopulse loop

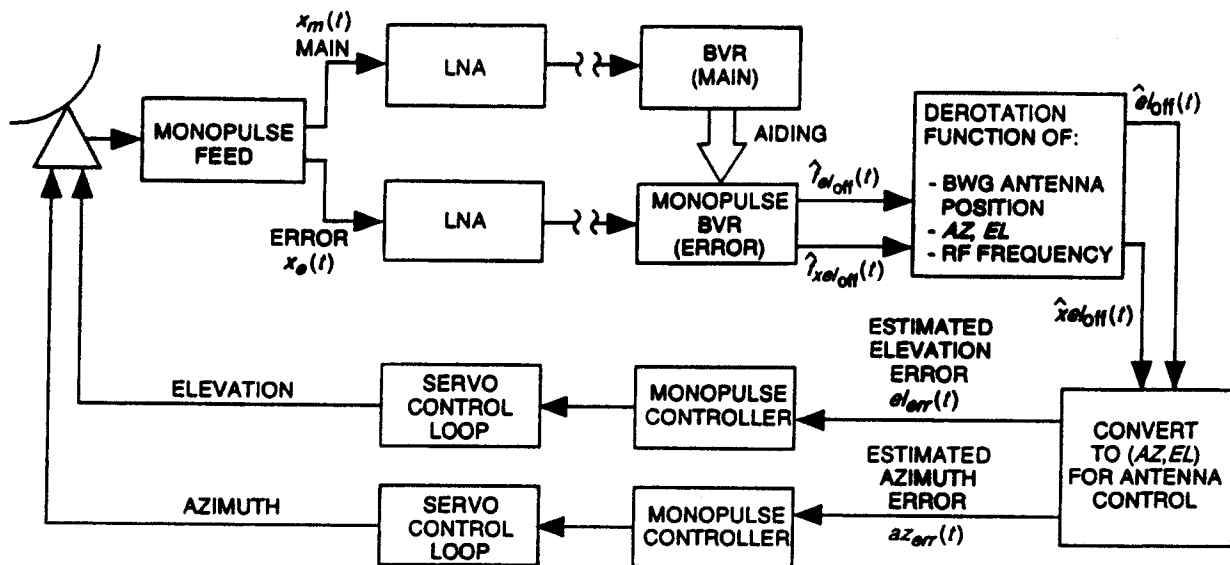


Fig. 1. The monopulse pointing design in the DSN 34-m beam-waveguide antennas.

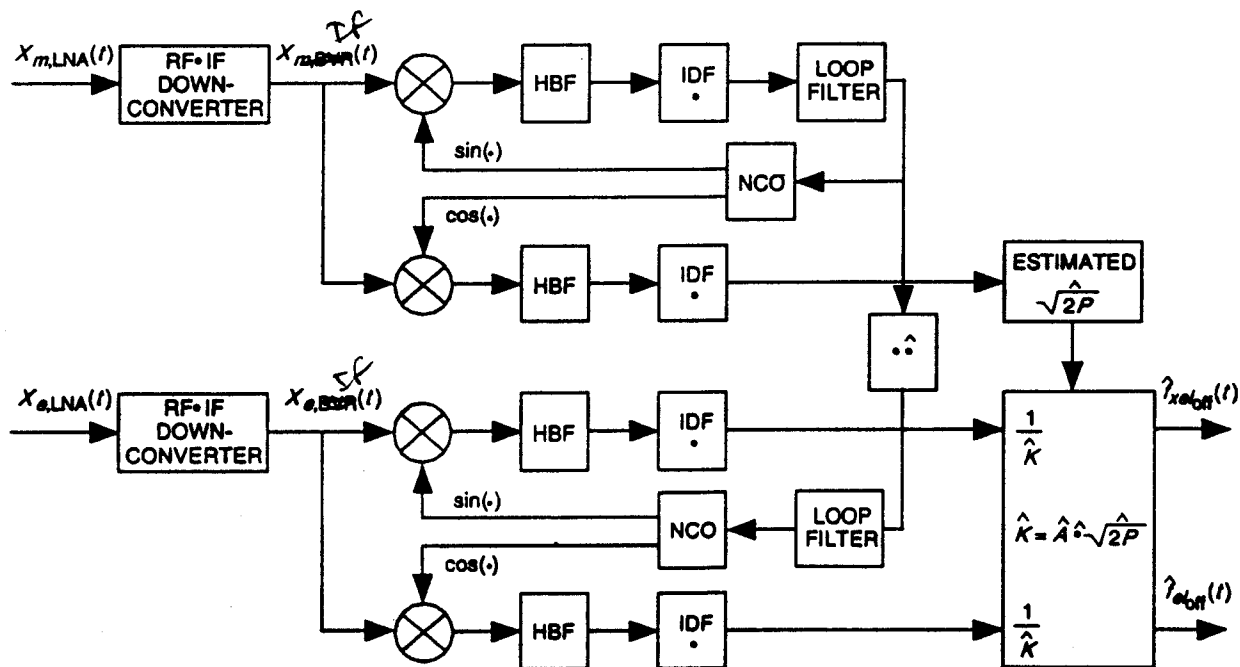


Fig. 2. The block diagram for receiver processing.

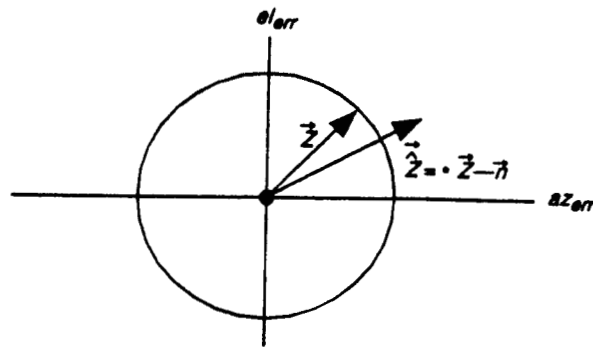


Fig. 3. The estimated pointing-error vector versus the true pointing-error vector.

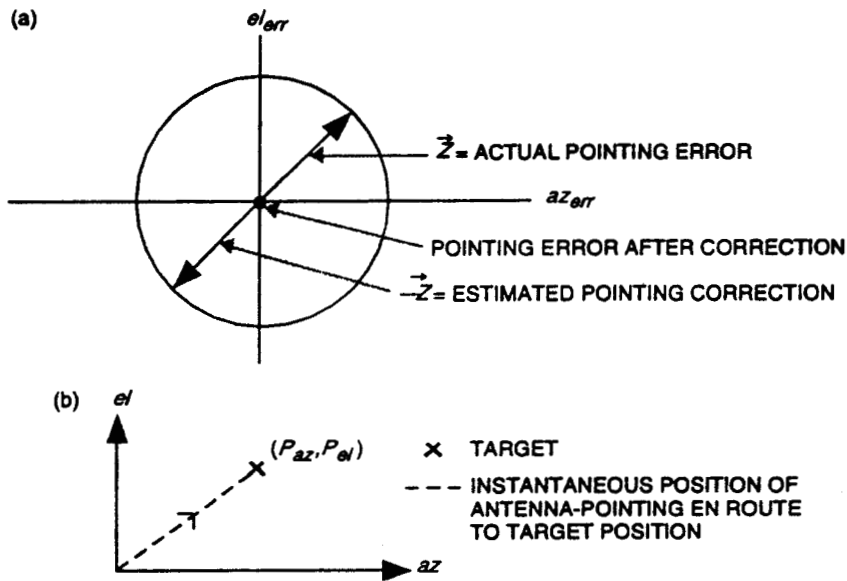


Fig. 4. The ideal case for pointing-error correction: (a) perfect pointing-error correction in two-dimensional space and (b) ideal transient response in target acquisition.

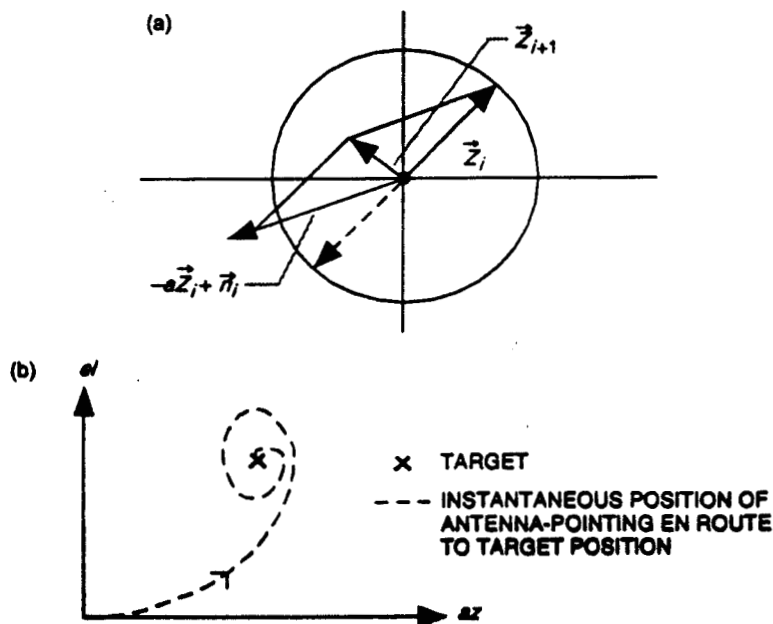


Fig. 5. The non-ideal case for pointing-error correction: (a) imperfect pointing-error correction in two-dimensional space and (b) non-ideal transient response in target acquisition.

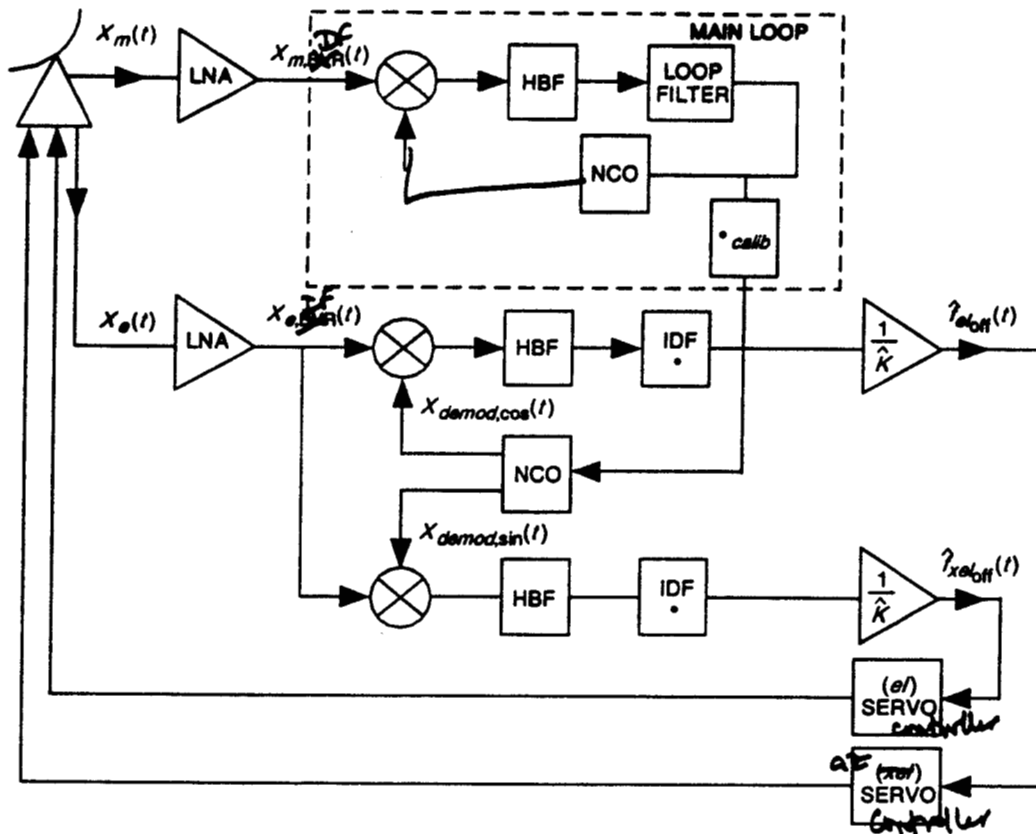


Fig. 6. The monopulse loop block diagram.

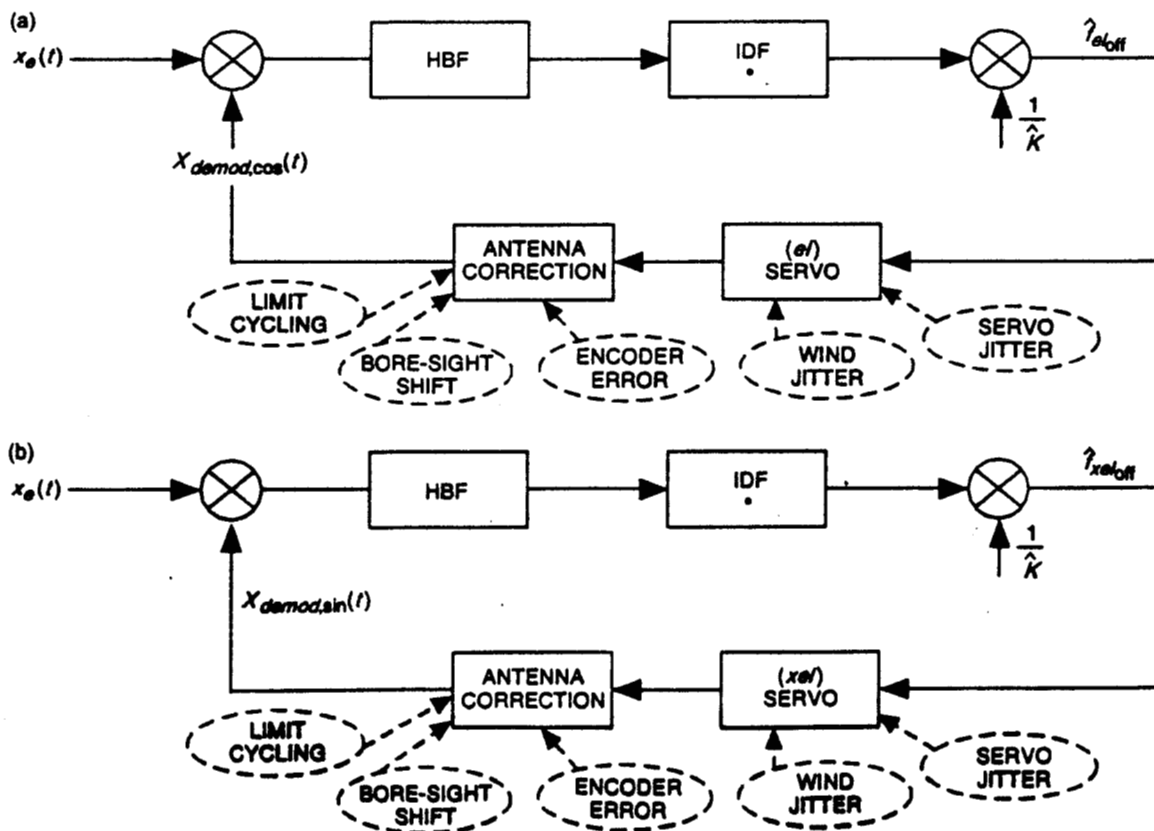


Fig. 8. Independent monopulse loop models: (a) elevation tracking loop and (b) cross-elevation tracking loop.

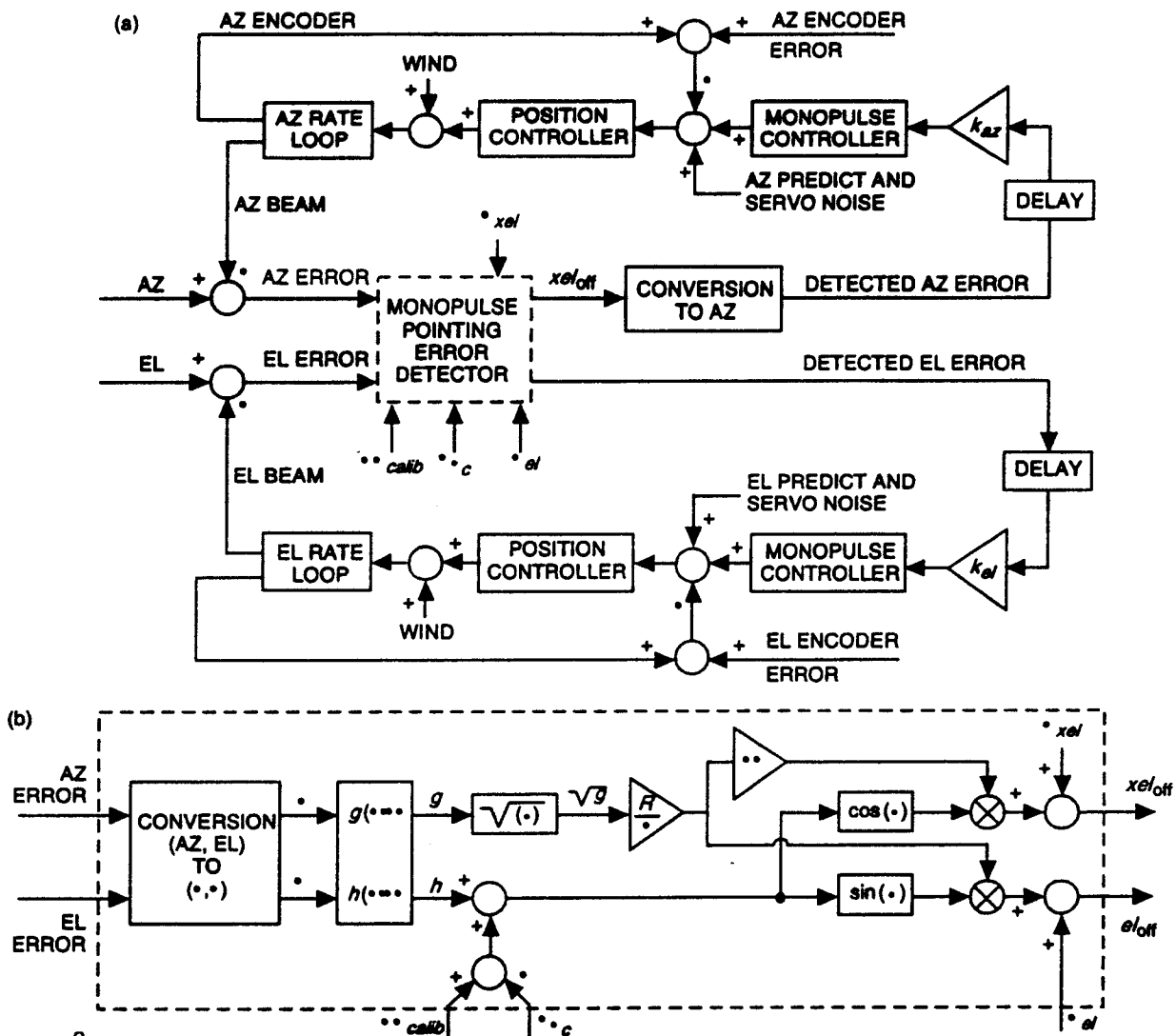


Fig. 8. Block diagrams of (a) the nonlinear monopulse control model and (b) the monopulse pointing-error detector.



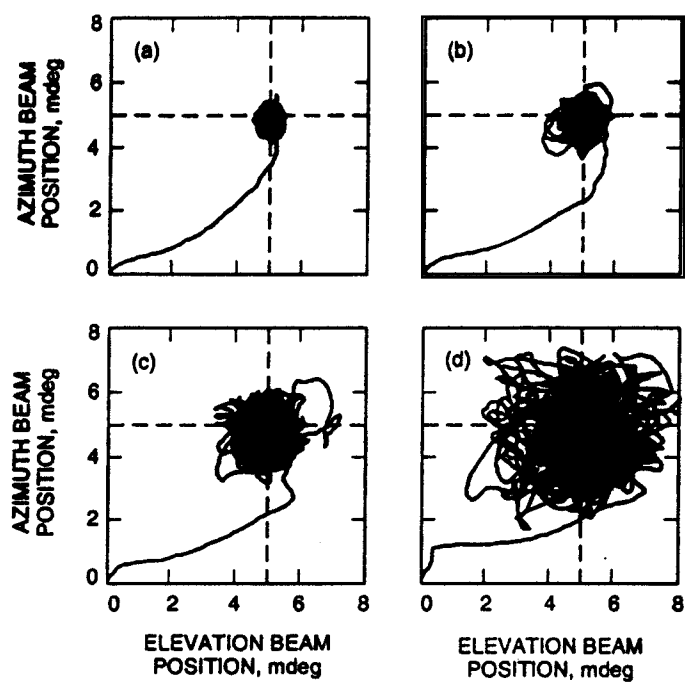


Fig. 12. Pointing as a function of time during acquisition and lock for a  $P_{s,m} / N_{0,s}$  of (a) 40 dB-Hz, (b) 27 dB-Hz, (c) 23 dB-Hz, and (d) 17 dB-Hz.

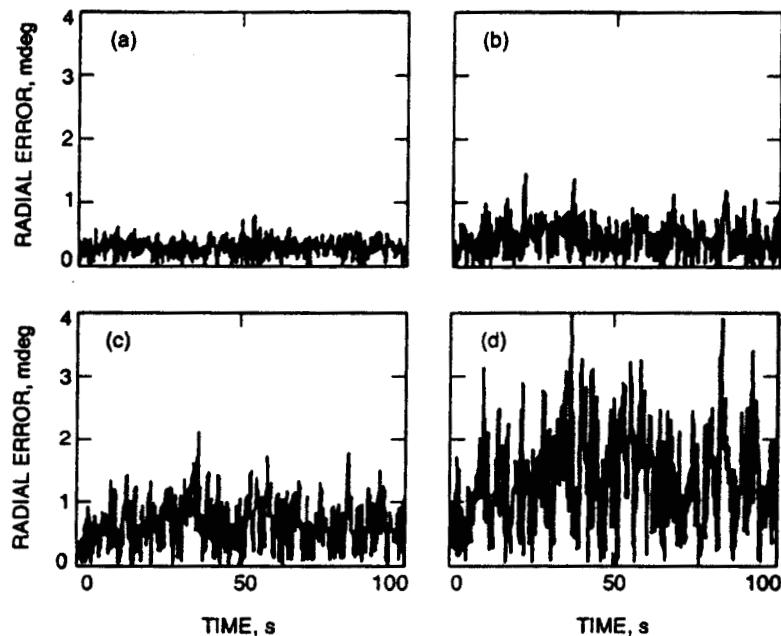


Fig. 10. Pointing radial error as a function of time for a  $P_{c,m}/N_{0,e}$  of (a) 40 dB-Hz, (b) 27 dB-Hz, (c) 23 dB-Hz, and (d) 17 dB-Hz.

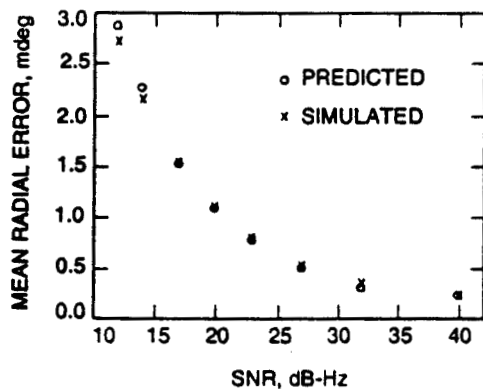


Fig. 11. The predicted compared to the simulated mean radial error for a 35-dB null depth as a function of SNR  $= P_{c,m}/N_{0,e}$ .

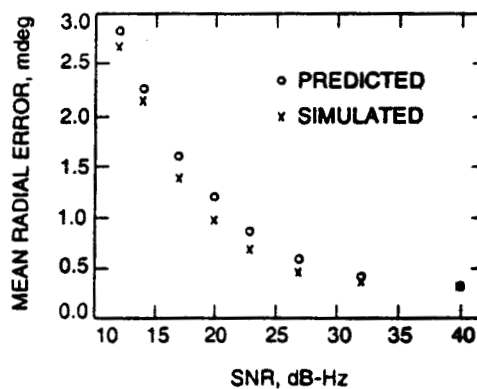
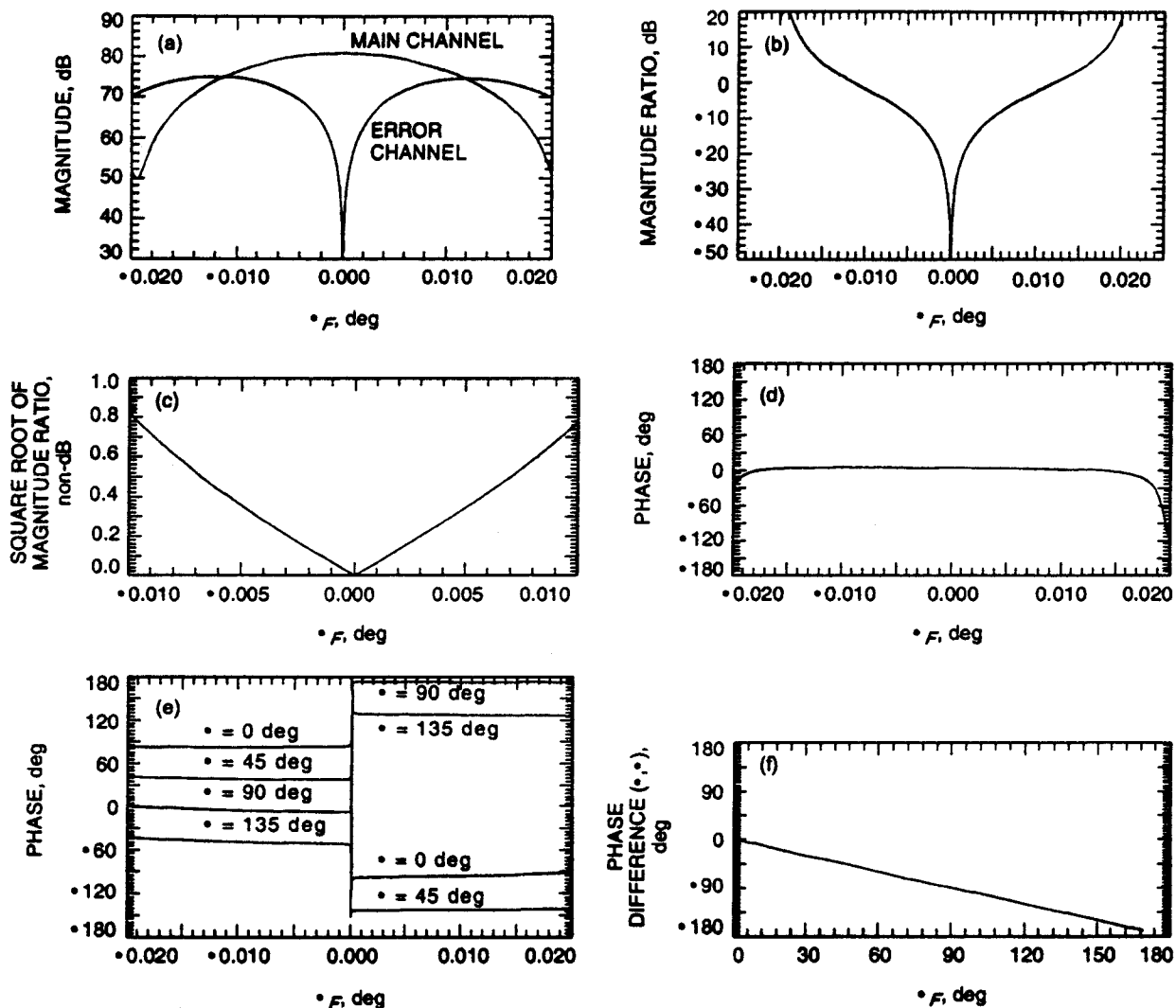


Fig. 12. The predicted compared to the simulated mean radial error for a 15-dB null depth as a function of SNR  $= P_{c,m}/N_{0,e}$ .



**A**  
**Fig. 8-1. Ideal antenna patterns:** (a) the magnitude of the main- and error-channel patterns versus  $\theta$ , (b)  $g(\theta, \theta)$ , the magnitude of the ratio of the main-channel over the error-channel patterns versus  $\theta$  (approximately constant as a function of  $\theta$ ), (c)  $\sqrt{g(\theta, \theta)}$  (non-dB), about  $\pm 10$  mdeg  $< \theta < \pm 10$  mdeg (ideal case), (d) the phase of the main channel versus  $\theta$ , (e) the phase of the error channel versus  $\theta$ , and (f)  $h(\theta, \theta)$ , the phase difference between the main- and error-channel patterns (approximately constant as a function of  $\theta$ ).

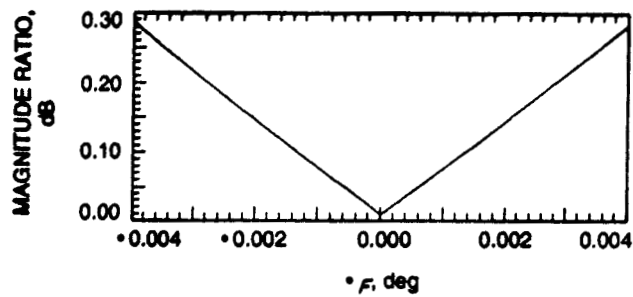


Fig. 8-2.  $\sqrt{g'(\theta_F, \theta_F)}$  (non-dB), about  $\pm 10$  mdeg  $\ll \pm 10$  mdeg (non-ideal case); null depth = 15 dB.

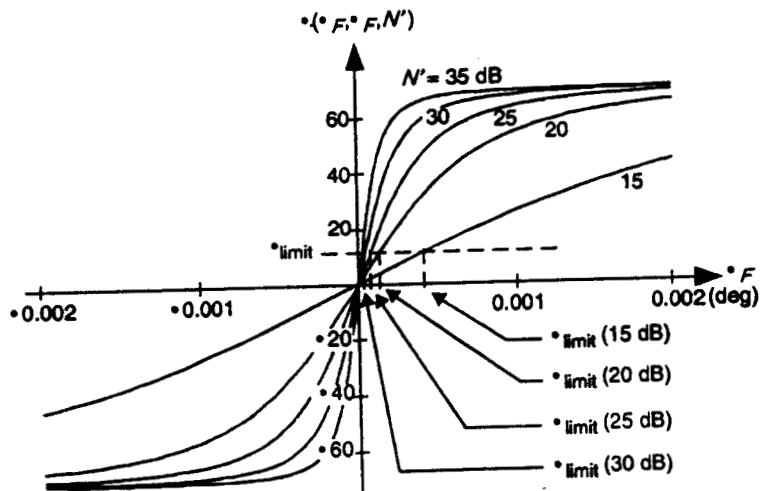


Fig. 8-3.  $\theta(\theta_F, \theta_F)$  versus  $\theta_F$  for decreasing values of  $N'$  dB (null depth).

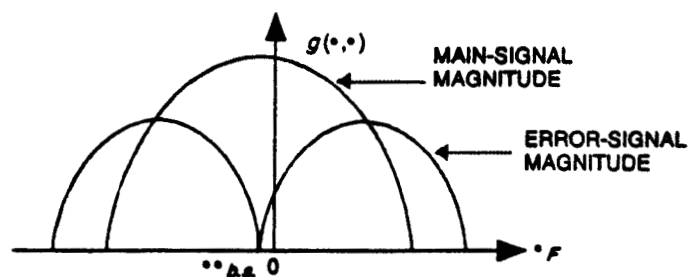


Fig. 8-4. Bore-sight shift: offset between the null depth and the RF peak.